

# The vorticity versus the scalar criterion for the detection of the turbulent/non-turbulent interface

Markus Gampert, Jonas Boschung†, Fabian Hennig, Michael Gauding and Norbert Peters

Institute for Combustion Technology, RWTH Aachen University, Templergraben 64, Aachen, Germany

(Received 7 August 2013; revised 9 May 2014; accepted 15 May 2014;  
first published online 10 June 2014)

Based on a direct numerical simulation (DNS) of a temporally evolving mixing layer, we present a detailed study of the turbulent/non-turbulent (T/NT) interface that is defined using the two most common procedures in the literature, namely either a vorticity or a scalar criterion. The different detection approaches are examined qualitatively and quantitatively in terms of the interface position, conditional statistics and orientation of streamlines and vortex lines at the interface. Computing the probability density function (p.d.f.) of the mean location of the T/NT interface from vorticity and scalar allows a detailed comparison of the two methods, where we observe a very good agreement. Furthermore, conditional mean profiles of various quantities are evaluated. In particular, the position p.d.f.s for both criteria coincide and are found to follow a Gaussian distribution. The terms of the governing equations for vorticity and passive scalar are conditioned on the distance to the interface and analysed. At the interface, vortex stretching is negligible and the displacement of the vorticity interface is found to be determined by diffusion, analogous to the scalar interface. In addition, the orientation of vortex lines at the vorticity and the scalar based T/NT interface are analyzed. For both interfaces, vorticity lines are perpendicular to the normal vector of the interface, i.e. parallel to the interface isosurface.

**Key words:** mixing, shear layer turbulence, turbulent flows

---

## 1. Introduction

In free shear flows such as mixing layers, wakes and jet flows, different flow regimes are observed, namely a fully turbulent region and a laminar outer flow, the two being separated by the so-called turbulent/non-turbulent (T/NT) interface. The fully turbulent region is associated with vortical flow, while irrotational velocity fluctuations are found in the non-turbulent flow outside the interface. Thus, a change in the character of the fluctuations from vortical ( $\boldsymbol{\omega}$  is non-zero, where  $\boldsymbol{\omega} = \nabla \times \boldsymbol{u}$  is the vorticity) to irrotational ( $\boldsymbol{\omega}$  is negligible) is observed, see Bisset, Hunt & Rogers (2002). Across this thin interface layer all major changes between the outer flow

† Email address for correspondence: [j.boschung@itv.rwth-aachen.de](mailto:j.boschung@itv.rwth-aachen.de)

and the fully turbulent flow take place, including those of vorticity, enstrophy or any transported passive scalar. The interaction between the two flows at the interface leads to an exchange of mass, momentum and scalar quantities. At the largest scales, this corresponds to the physical mechanism of entrainment.

In terms of coherent structures identified in various types of turbulent flows, cf. Kline *et al.* (1967), Brown & Roshko (1974), Dimotakis, Miake-Lye & Papantoniou (1983), Hussain (1986), Liepmann & Gharib (1992) and Cannon, Champagne & Glezer (1993), the question arises of how the local topology of these flows may be described from a structural point of view and how their impact may be described physically, as well as quantified in terms of turbulence statistics. Townsend (1956, 1966, 1987) was the first to bring forth the idea of describing so-called coherent eddies using two-point correlations, cf. Grant (1958). Recently, Marusic & Adrian (2011) gave a more precise definition of these coherent structures and the observed organized motion. Following the investigations of Perry & Chong (1982), Marusic & Perry (1995) and Nickels & Perry (1996), Philip & Marusic (2012) used a random collection of coherent large-scale eddies to describe first- and second-order statistics in axisymmetric jets and wakes. The latter authors further investigated the physical importance of these large-scale eddies in the local entrainment process that describes the advance of the T/NT interface layer into the irrotational fluid normal to its own surface, cf. Bisset *et al.* (2002). While Liepmann & Gharib (1992) and Yoda, Hesselink & Mungal (1994) discuss the impact of these large-scale eddies and the motion of large-scale vortices (engulfment) on the entrainment process, Mathew & Basu (2002), Westerweel *et al.* (2005) and Westerweel *et al.* (2009) suggest that small-scale eddy motions (nibbling) acting on the T/NT interface layer are the dominant physical mechanism.

These nibbling eddies are of major importance for the dynamics of the interface layer, see Hunt *et al.* (2011) for a review of recent investigations. Detailed spatial analyses of this region have been made experimentally, cf. Westerweel *et al.* (2002, 2009) and Holzner *et al.* (2007*a,b*), and numerically, cf. da Silva & Pereira (2008), da Silva & Taveira (2010) and da Silva & Dos Reis (2011), giving deeper insight into the vorticity dynamics close to the T/NT interface.

Bisset *et al.* (2002) note that the components of the vorticity exhibit a jump at the T/NT interface. Westerweel *et al.* (2009) observed such a jump also for the streamwise velocity and a passive scalar across the T/NT interface. Holzner *et al.* (2007*a*, 2008) examined the dynamics of enstrophy and strain near the T/NT interface. They found intense dissipation  $\varepsilon$  outside the turbulent region and observed that near the T/NT interface viscosity causes an increase of the total enstrophy. Further insight was gained by Holzner *et al.* (2008), who observed that viscous diffusion is responsible for the viscous contribution to the enstrophy, while the enstrophy viscous dissipation remains negative.

In da Silva & Pereira (2008) the second and third invariants  $Q$  and  $R$  of the velocity gradient tensor  $\partial u_i/\partial x_j$  are examined which gives information about the local behaviour of streamlines relative to the flow, see Chong, Perry & Cantwell (1990). They found that at the T/NT interface, saddle topologies corresponding to a relative straining motion of the flow dominate and that the well-known 'tear drop' shape in the  $Q$ - $R$  map is not present, but appears only about one Taylor microscale  $\lambda$  into the turbulent region. In addition, Westerweel *et al.* (2011) examined the temperature field of a non-isothermal jet and observed a good agreement of the statistics with those obtained from the investigation of concentration and axial momentum, see Westerweel *et al.* (2005), Holzner *et al.* (2007*a*), da Silva & Pereira (2008), Holzner *et al.* (2008)

and Westerweel *et al.* (2009). Furthermore, da Silva & Pereira (2008) argue, based on scaling arguments involving the viscosity and the rate of strain, that in the presence of a mean shear, the characteristic length scale  $\delta$  associated with the thickness of the interface scales with the Taylor microscale  $\lambda$ .

In a previous work, Gampert *et al.* (2013a), the contribution of the T/NT interface to the mixture fraction probability density function (p.d.f.)  $P(\phi)$ , the mixture fraction  $\phi$  being a conserved (i.e. passive) scalar used in combustion, at various axial and radial locations of a turbulent jet has been examined. It was concluded that the T/NT interface and its contributions to the mixture fraction p.d.f. are of major importance particularly in the early part of the jet. In addition, the thickness  $\delta$  of the scalar T/NT interface was found to scale with the Taylor microscale  $\lambda$  in the range of Taylor-microscale-based Reynolds numbers  $Re_\lambda = 60\text{--}140$ , using the mixture fraction profile in the interface normal direction.

In addition, Gampert *et al.* (2014) studied numerically this turbulent jet flow using two large-eddy simulations (LES) simulations with different resolutions and compared their results to the experimental data. To this end, they examined the mixture fraction p.d.f. at various axial and radial positions in the jet flow and observed considerable discrepancies in the flow region where the contributions of the T/NT interface layer to the p.d.f. are dominant. The agreement between experiments and simulation was more satisfactory for the p.d.f. with the finer LES. In particular, it was found that the generally reported sharp jump of the scalar value across the interface, cf. Westerweel *et al.* (2009) and Gampert *et al.* (2013a), is less distinct in the LES results, but rather diffused in the radial direction. Based on these results it was concluded that current subgrid models need to be improved for LES to predict this region of the flow properly.

Direct numerical simulation (DNS) analyses of the region of the T/NT interface were performed by Mellado, Wang & Peters (2009), who investigated a temporally evolving shear layer by using gradient trajectories. They applied this analysis to partition the scalar field into a fully turbulent zone, a zone containing the T/NT interface and the outer laminar flow. They examine the probabilities in these three zones at different locations in the shear layer and investigate the scalar p.d.f. and the conditional scalar dissipation rate in the zones in the presence of external intermittency. This approach was adopted by Gampert *et al.* (2013b), where zonal statistics of the mixture fraction p.d.f.  $P(\phi)$  as well as the scalar difference along a scalar gradient trajectory  $\Delta\phi$  and its mean scalar value  $\phi_m$  were examined based on experimentally obtained scalar fields in a jet flow. In addition, Gampert *et al.* (2013b) reconstructed  $P(\phi)$  from zonal gradient trajectory statistics of the joint p.d.f.  $P(\phi_m, \Delta\phi)$  and observe a very good qualitative and quantitative agreement with the experimental data.

Although most of the above studies use similar approaches to detect the T/NT interface and report results that agree for different fields, a detailed comparison of results stemming from the various ways to define the instantaneous position of the interface is still missing. The most common ways to detect the interface are either based on a scalar field or the vorticity/enstrophy. The former approach uses a threshold defined from the p.d.f. of a scalar quantity and was originally presented by Prasad & Sreenivasan (1989) and was recently applied successfully, for instance, by Holzner *et al.* (2007a), Westerweel *et al.* (2009) and Gampert *et al.* (2013a). In contrast, Bisset *et al.* (2002) and da Silva & Pereira (2008) used the absolute value of vorticity  $\omega$  (with  $\omega = |\boldsymbol{\omega}| = (\omega_i \omega_i)^{1/2}$ ) to find the interface position. Furthermore, a completely different way has been presented by Mellado *et al.* (2009) using gradient trajectories in a scalar field to obtain the region in which the flow turns from laminar to fully turbulent.

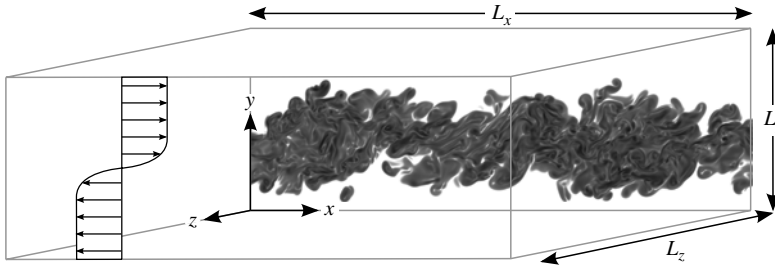


FIGURE 1. Sketch of the temporally evolving mixing layer geometry and the mean velocity profile.

In this work, we intend to present a comprehensive study of the T/NT interface, in which the different approaches described above are applied and compared critically. This will allow a conclusion on the universality of results obtained for instance related to the T/NT interface detected based on a threshold procedure in the enstrophy field, when transferred to an interface stemming from a passive scalar. To this end, we have performed a DNS of the velocity field and a passive scalar in a temporally evolving mixing layer. In § 2, we present details of this DNS based on which we examine the topology of various scalar fields in § 3. Conventional statistics of the T/NT interface (using either a passive scalar or an enstrophy criterion for its detection) are examined and compared in § 4. In § 5, we investigate the orientation of streamlines and vortex lines. The paper is concluded with a brief summary in § 6.

### 2. Direct numerical simulation

A DNS of a temporally evolving mixing layer has been conducted. A schematic illustration of the computational domain is given in figure 1. The DNS is performed by solving the non-dimensional unsteady incompressible Navier–Stokes equations using the velocity difference  $\Delta U$  between the upper and lower boundary  $\Delta U = u_1(y = L_y) - u_1(y = 0)$  and the vorticity thickness  $\delta_{\omega 0}$  for non-dimensional quantities. Additionally an advection–diffusion equation is solved for a passive scalar with unity Schmidt number  $Sc$ . The non-dimensional equations thus are

$$\frac{\partial u_i}{\partial x_i} = 0, \tag{2.1}$$

$$\frac{\partial u_i}{\partial t} = -\frac{\partial}{\partial u_j}(u_i u_j) + \frac{1}{Re_{\delta,0}} \frac{\partial^2 u_i}{\partial x_j^2} - \frac{\partial p}{\partial x_i}, \tag{2.2}$$

$$\frac{\partial \phi}{\partial t} = -u_i \frac{\partial \phi}{\partial x_i} + \frac{1}{Pe_{\delta,0}} \frac{\partial^2 \phi}{\partial x_i^2}, \tag{2.3}$$

$$\frac{\partial \omega_i}{\partial t} = -u_j \frac{\partial \omega_i}{\partial x_j} + \omega_j \frac{\partial u_i}{\partial x_j} + \frac{1}{Re_{\delta,0}} \frac{\partial^2 \omega_i}{\partial x_j^2}, \tag{2.4}$$

where  $Pe_{\delta,0} = Sc Re_{\delta,0}$ . The initial vorticity thickness is given by

$$\delta_{\omega 0} = \delta_{\omega}(t = 0) = \frac{\Delta U}{(d\langle u_1 \rangle / dz)_{max}} \Big|_{t=0} \equiv 1, \tag{2.5}$$

$t$	$Re_\lambda$	$\lambda$	$\delta_m$	$\delta_\omega$	$Re_\delta$	$\eta$	$\eta/\Delta x$
160	86.5	0.92	2.37	11.53	703.7	0.051	0.69
186	93.9	1.00	2.71	14.23	868.1	0.052	0.71
211	98.9	1.05	3.03	16.72	1019.9	0.054	0.73

TABLE 1. Simulation parameters.

i.e. set to unity for the present simulation. The momentum thickness is defined as

$$\delta_m = \int_0^{L_y} \left( \frac{1}{4} - \frac{\langle u_1 \rangle^2}{\Delta u} \right) dy, \quad (2.6)$$

where  $\delta_{m0} = \delta_m(t=0)$ , and  $\langle \rangle$  denote the ensemble average.

The velocity profile is initialized following Pantano & Sarkar (2002) by

$$\langle u_1(y) \rangle = \frac{\Delta U}{2} \tanh \left( \frac{1}{2} \left( y - \frac{L_y}{2\delta_{\omega 0}} \right) \right), \quad (2.7)$$

$$\langle u_2(y) \rangle = \langle u_3(y) \rangle = 0, \quad (2.8)$$

while the scalar value is one at the upper boundary and zero at the lower boundary and is initialized according to

$$\langle \phi(y) \rangle = \frac{1}{2} \tanh \left( \frac{1}{2} \left( y - \frac{L_y}{2\delta_{\omega 0}} \right) \right). \quad (2.9)$$

In order to obtain a high accuracy, spatial derivatives are calculated by a sixth-order finite-difference compact scheme introduced by Lele (1992). The temporal integration is performed using a fourth-order Runge–Kutta method. The Poisson equation is solved in spectral space by adapting a Helmholtz equation. The initial velocity profile, see (2.7) and (2.8), is superposed with a broadband random Gaussian velocity field derived from a one-dimensional turbulent energy spectrum to facilitate laminar–turbulent transition. This energy spectrum is proportional to  $\kappa^2 \exp(\kappa/\kappa_0)$ , with  $\kappa$  being the wavenumber with a peak at the wavelength  $\kappa_0 = 3\delta_{\omega 0}$  comparable to the energy spectrum imposed by Mellado *et al.* (2009). The initial turbulence intensity is set to 6%. The initial Reynolds number  $Re_{\delta,0} = \Delta U \delta_{\omega 0} / \nu$ , based on the vorticity thickness, is  $Re_{\delta,0} = 672$ . The streamwise  $x$  and the spanwise  $z$  boundary conditions are periodic. The cross-stream boundaries are determined by the free-slip condition.

The size of the computational domain is given by  $L_x = 24\pi$ ,  $L_y = 18\pi$  and  $L_z = 18\pi$ . For an appropriate resolution of the mixing layer, the grid is equidistant ( $\Delta x = \Delta y = \Delta z$ ) in the core region (between  $0.25L_y$  and  $0.75L_y$ ). Grid spacing coarsens towards the cross-stream boundaries. Grid spacing in the streamwise and spanwise direction is constant over the complete domain. The domain is discretized by  $1024 \times 768 \times 768$  ( $N_x \times N_y \times N_z$ ) grid points. The resolution in the core region is given by  $\Delta x \leq 1.46\eta$  with the Kolmogorov scale  $\eta = \nu^{3/4} \varepsilon^{-1/4}$  in order to properly resolve small-scale turbulence in the mixing layer. In table 1 details of the simulation parameters are given, showing that the Taylor-based Reynolds number ranges up to  $Re_\lambda \approx 86.5$  and the vorticity thickness increases up to a value of  $\delta_\omega = 11.53$ .

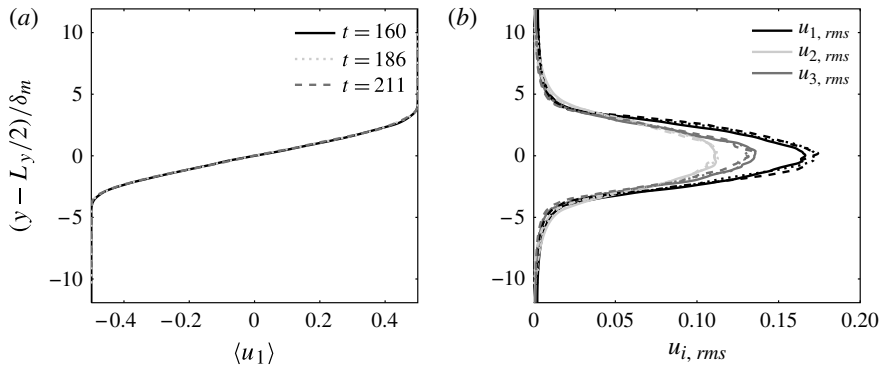


FIGURE 2. (a) Mean of velocity field component  $u_1$  and (b) r.m.s. of  $u_1$ ,  $u_2$  and  $u_3$  conditioned on the cross-stream direction  $y$  for  $t=160$  (solid lines),  $t=186$  (dotted lines),  $t=211$  (dashed lines).

Finally, the DNS was validated against corresponding studies from Rogers & Moser (1994), Pantano & Sarkar (2002) and Mellado *et al.* (2009). In agreement with these, we observe after the initial transient that the momentum thickness growth rate approaches  $0.018\Delta U$ , a value comparable to  $0.016\Delta U$  reported by Rogers & Moser (1994) and to  $0.018\Delta U$  reported by Pantano & Sarkar (2002) and Mellado *et al.* (2009). Furthermore, the integral across the layer of  $\langle \varepsilon \rangle$  is constant after the initial transient. In particular, the data we use in the present study are taken from the self-similar state of the mixing layer. Figures 2(a,b) show the conditional mean value of the velocity field component  $u_1$  and the root-mean-squares (r.m.s.) of the components  $u_1$ ,  $u_2$  and  $u_3$  at  $t=160$ ,  $t=186$  and  $t=211$ . Clearly, the profiles collapse if normalized by the momentum thickness  $\delta_m$ , indicating the self-similar state. The conditional mean of the passive scalar  $\phi$  also collapses, when the same normalization is used. The statistics presented in the following sections have been evaluated using the single dataset at  $t=160$ .

### 3. Scalar field topology

A visualization of the flow is presented in figure 3, where the passive scalar field  $\phi$  is depicted through two planar  $xOz$  cuts, one being the centreplane and the other at the edge of the mixing region at  $y/\delta = 22.19$  (note that this position will in the next section be found to be the mean interface location). The corresponding scalar dissipation rate  $\chi$ , defined as

$$\chi = 2D (\partial\phi/\partial x_i)^2, \tag{3.1}$$

where  $D$  is a molecular diffusion coefficient (note that  $D = \nu$ , as  $Sc = 1$ ), is shown in figure 4 in logarithmic scale and with a colour grade varying from blue (lowest value) to red (highest value), clearly illustrating the structure in the passive scalar and its dissipation field. There are large patches of the order of the integral scale in which the scalar amplitudes are roughly constant. The boundaries of these regions, however, are very sharp and convoluted. Naturally,  $\chi$  has large values at the boundary forming sheets of high scalar dissipation between such adjacent patches as expected from (3.1). This structure as well as the observable structure of  $\chi$  is much more pronounced for the centreplane, while in the outer region many non-turbulent regions are present.

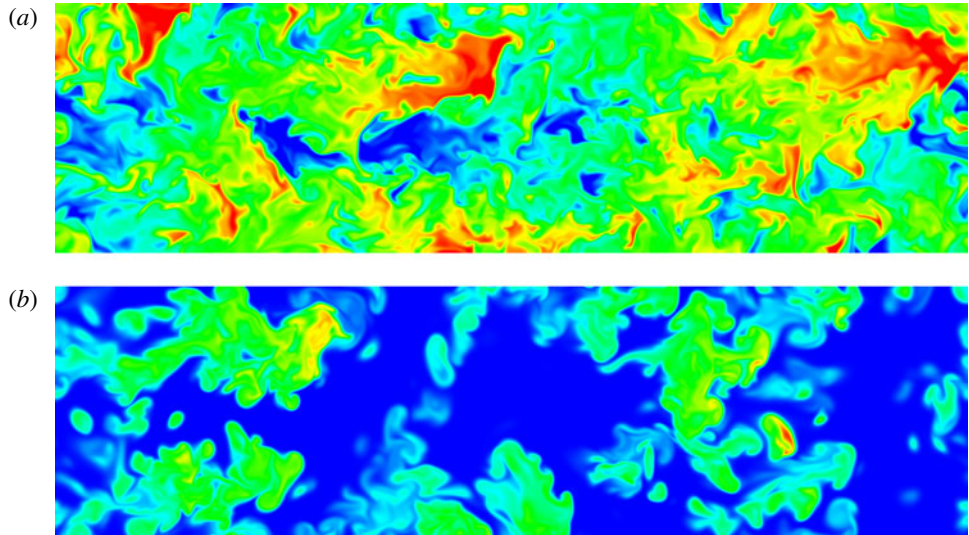


FIGURE 3. Passive scalar  $\phi$ , colour scale starting at blue, increasing in the sequence green–yellow–red: (a)  $xOz$  plane at  $y/\delta = 28.27$  (centreplane), (b)  $xOz$  plane at  $y/\delta = 22.19$  (mean position of lower interface). The size of the cut planes equals  $L_x \times 0.36L_z = 24\pi \delta_{\omega 0} \times 6.48\pi \delta_{\omega 0}$ .

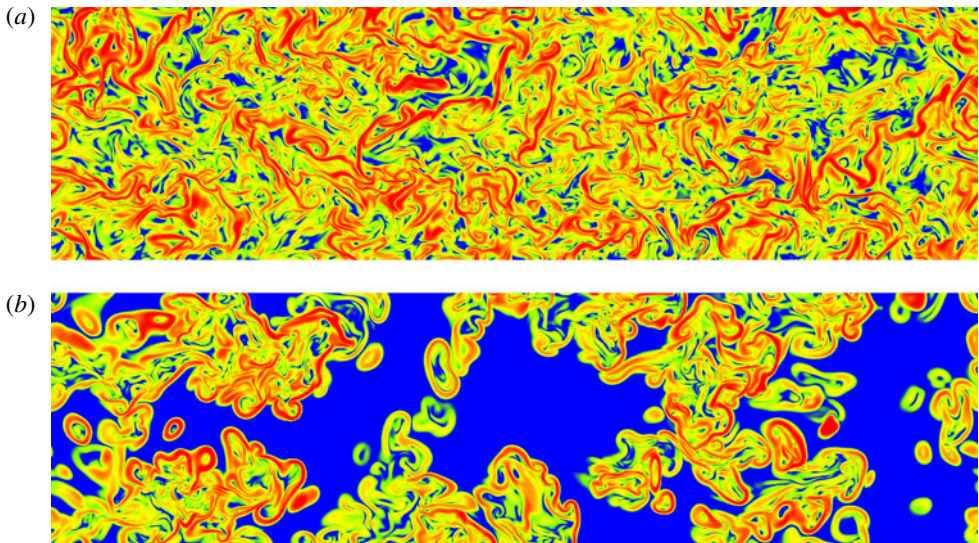


FIGURE 4. Logarithm of scalar dissipation rate  $\chi$ , colour scale starting at blue, increasing in the sequence green–yellow–red: (a)  $xOz$  plane at  $y/\delta_{\omega 0} = 28.27$  (centreplane), (b)  $xOz$  plane at  $y/\delta_{\omega 0} = 22.19$  (mean position of lower interface). The size of the cut planes equals  $L_x \times 0.36L_z = 24\pi \delta_{\omega 0} \times 6.48\pi \delta_{\omega 0}$ .

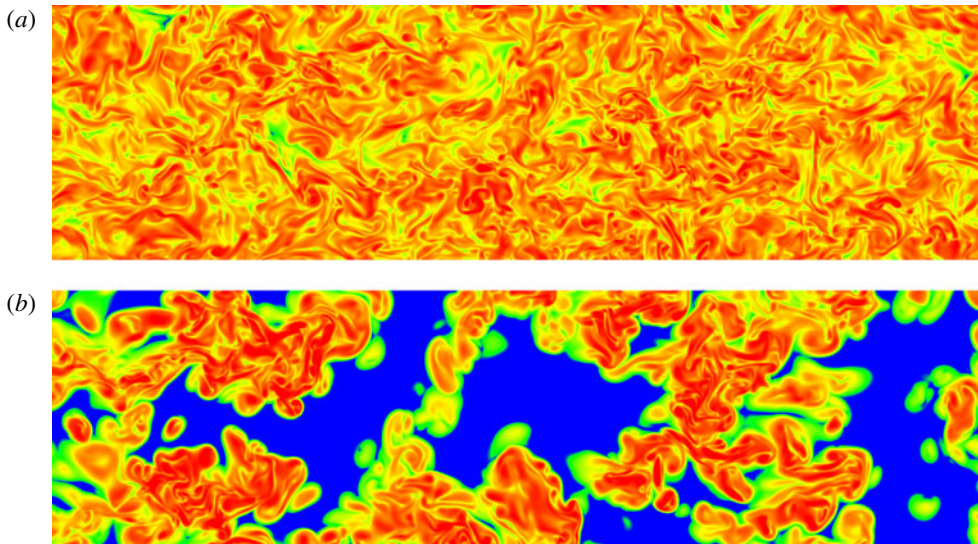


FIGURE 5. Logarithm of the absolute value of vorticity  $\omega$ , colour scale starting at blue, increasing in the sequence green–yellow–red: (a)  $xOz$  plane at  $y/\delta_{\omega 0} = 28.27$  (centreplane), (b)  $xOz$  plane at  $y/\delta_{\omega 0} = 22.19$  (mean position of lower interface). The size of the cut planes equals  $L_x \times 0.36L_z = 24\pi \delta_{\omega 0} \times 6.48\pi \delta_{\omega 0}$ .

Figure 5 shows the local absolute value of vorticity  $\omega$ , i.e. the square root of enstrophy, at different horizontal  $xOz$  planes on the centreplane and at the edge of the mixing region, in logarithmic scale and with a colour grade varying again from blue (lowest value) to red (highest value). In agreement with previous works, we observe a lamellar character for the field with strongly swirling tube/worm-like structures, cf. Kerr (1985), Ashurst *et al.* (1987), Jimenez *et al.* (1993) and Vincent & Meneguzzi (1994). These worms had been imagined to be embedded in structureless weak and nearly Gaussian vorticity, cf. Jimenez *et al.* (1993). Ruetsch & Maxey (1991), however, showed that within this structureless vorticity regions of high dissipation exist that tend to surround the high-enstrophy worms, are topologically sheet-like and seem to be organized into distinct structures, cf. Tsinober, Shtilman & Vaisburd (1997). Regions of weaker enstrophy have also been found to be far more dynamically important, especially with respect to the enstrophy production, cf. Tsinober, Ortenberg & Shtilman (1999).

The sheet-like structure of the scalar dissipation rate field  $\chi$  has already been shown in two- and three-dimensional measurements by Buch & Dahm (1996, 1998), Su & Clemens (2003), Frank & Kaiser (2010) and Patton *et al.* (2012) and in DNS by Watanabe & Gotoh (2004) and Kushnir, Schumacher & Brandt (2006). External intermittency is represented in figures 3 and 4 by the alternation of blue free-stream and coloured turbulent zones. The ratios between the area occupied by the coloured zone and the total area in the horizontal planes are precisely the intermittency factors  $\gamma(y/\delta_{\omega 0} = 28.27)$  and  $\gamma(y/\delta_{\omega 0} = 22.19)$ , see Townsend (1948, 1949). The former has a large intermittency factor close to one, although regions of unmixed fluid are observed to reach the centreplane, cf. Gampert *et al.* (2013a) for similar observations in a jet flow, whereas the latter has a value of  $\gamma$  significantly smaller than one. Specifically, we find for the scalar interface  $\gamma^\phi(y/\delta_{\omega 0} = 28.27) = 0.9855$  in the centreplane and

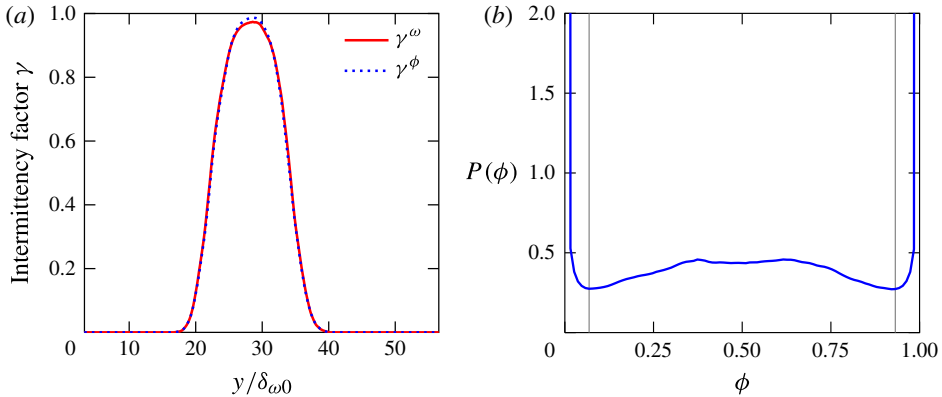


FIGURE 6. (Colour online) (a) Mean intermittency as a function of  $y/\delta_{\omega 0}$  and (b) p.d.f. of  $\phi$ , where grey lines indicate the threshold values  $\phi = 0.07$  (lower interface) and  $\phi = 0.93$  (upper interface).

$\gamma^\phi(y/\delta_{\omega 0} = 22.19) = 0.4721$  at the mean interface position, while in case of the vorticity interface,  $\gamma^\omega(y/\delta_{\omega 0} = 28.27) = 0.9723$  and  $\gamma^\omega(y/\delta_{\omega 0} = 22.19) = 0.4870$ . Thus, both criteria (or, more precisely, the chosen thresholds) result in very similar intermittency factors  $\gamma$ . This is also visualized in figure 6(a), where the mean of  $\gamma$  as evaluated for different  $xOz$  planes  $y/\delta_{\omega 0}$  is shown. In case of the vorticity criterion,  $\gamma$  equals the fraction of the flow for which  $\omega > 0.7 U/H$ , while for the passive scalar  $\phi_{lower} < \phi < \phi_{upper}$ , i.e. values of  $\phi$  between the interface thresholds as defined below are evaluated. We find a very good agreement for both measures of intermittency  $\gamma^\omega$  and  $\gamma^\phi$ . Small deviations occur only close to the centreplane.

From the scalar fields of  $\phi$ ,  $\omega$  and  $\chi$  shown in figures 3 to 4 one deduces a stronger resemblance between  $\chi$  and  $\omega$  than between  $\phi$  and  $\omega$ . This would suggest the use of  $\chi$  or  $\omega$  as a criterion for the detection of the T/NT interface rather than  $\phi$ . On the other hand,  $\phi$  is easier to measure than  $\chi$  and a criterion based on  $\phi$  could replace the criterion based on  $\omega$  for the detection of the T/NT interface, if it can be shown that both are equivalent.

#### 4. Conditional statistics of the T/NT interface

In this section, we will investigate and compare the T/NT interface and its conditional statistics based on the mixture fraction and the enstrophy field. To this end, in a first step the interface is detected using two different approaches. In a second step, we will compare the location of these different interfaces and in a last step examine whether the statistics conditioned on the interface exhibit any dependence on the detection method.

##### 4.1. Interface detection

As discussed in the introduction, there exist two ways that are commonly used to find the T/NT interface: the first one is based on a criterion involving the absolute value of vorticity  $\omega$  and the second one applies a procedure based on a threshold of a passive scalar. These two detection methods give the instantaneous realizations shown in figure 7(a) for the vorticity criterion and figure 7(b) for the interface obtained from the passive scalar. For easier wording, we will in the following refer to the first one as

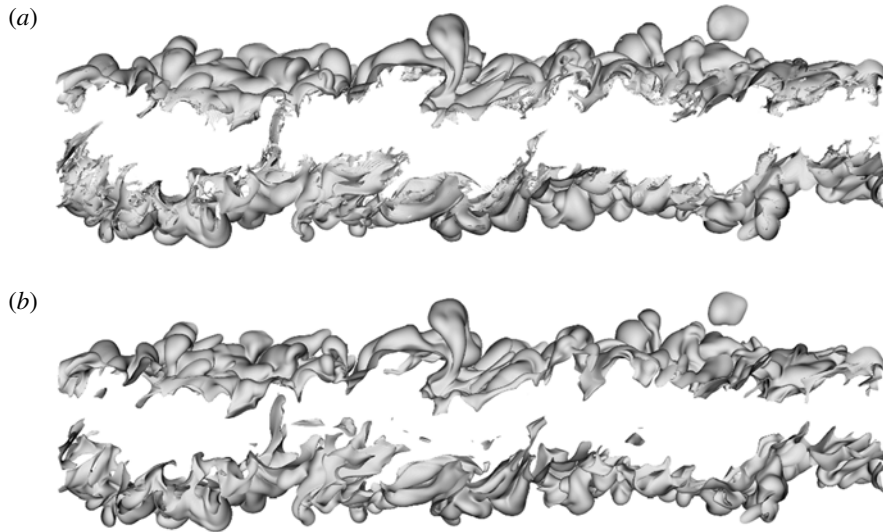


FIGURE 7. (a) Vorticity interface (isosurface  $\omega = 0.061$ ), (b) scalar interface (isosurface  $\phi = 0.93$  (upper) and  $\phi = 0.07$  (lower)).

the vorticity T/NT interface, and the second one as the scalar T/NT interface. However, before we focus on the qualitative and quantitative results associated with the two interfaces, a brief summary of the interface detection shall be given.

For the vorticity T/NT interface, we use the absolute value of the vorticity. This is used in the present work as a detection criterion, where the detection threshold of  $\omega = 0.7 U/H$  has been employed as suggested by Bisset *et al.* (2002) and da Silva & Pereira (2008) and similar to the approach of Mathew & Basu (2002), where  $U$  is a characteristic velocity of the flow configuration, for instance the exit velocity in a jet flow, and  $H$  denotes a characteristic length scale, which in the jet flow example might correspond to the nozzle diameter. In the present study, however, where a temporally evolving mixing layer is investigated,  $U$  is the velocity difference between upper and lower flows  $\Delta U$ , while  $H$  is the vorticity thickness  $\delta_\omega$ .

In contrast, the scalar T/NT interface is determined using the threshold procedure described by Prasad & Sreenivasan (1989), identifying the location of the interface by detecting the so-called envelope, cf. Westerweel *et al.* (2009). To this end, the threshold value at which the interface is located is determined if the histogram of the mixture fraction within the domain is bimodal for the local minimum value(s). For the present data, the p.d.f. is shown in figure 6(b). Clearly, a bimodal shape is found, resulting in threshold values of  $\phi = 0.07$  for the lower scalar interface and  $\phi = 0.93$  for the upper scalar interface, respectively.

Figure 7 shows a comparison of the vorticity and the scalar T/NT interfaces in terms of isosurfaces displaying strong convolutions with a large range of length scales. Some of the convolutions can be linked to the presence of large- and small-scale eddies lying just below the T/NT interface, whose surface is of fractal dimension, cf. Sreenivasan & Meneveau (1986). In the present case, the largest corrugations have length scales of the order of the Taylor microscale in agreement with the observations described by Taveira & da Silva (2013).

A planar cut through the  $xOy$  plane is shown in figure 8. In figure 8(a), the greyscale coding (where the values increase from white to black) indicates the

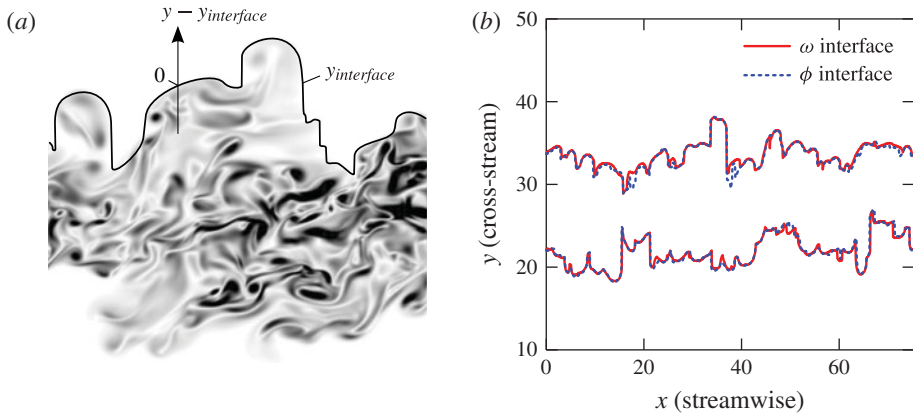


FIGURE 8. (Colour online) (a) Absolute value of vorticity  $\omega$  in the  $xOy$  plane. (b) Comparison of the position of the vorticity and scalar interface in the  $xOy$  plane.

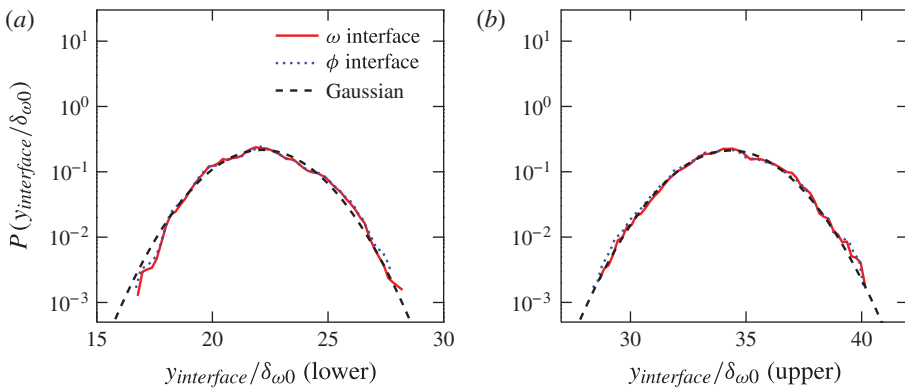


FIGURE 9. (Colour online) P.d.f. of the location of the vorticity and the scalar upper (a) and lower (b) T/NT interface.

absolute value of vorticity together with the corresponding vorticity T/NT interface. In addition, the coordinate system, as seen in figure 8(a), is attached to the interface, i.e. it is moving relative to the interface, and is used in §4.2 to compute conditional mean profiles across the interface. Furthermore, a comparison of the scalar and vorticity interfaces is given in figure 8(b), where instantaneous contours of the two interfaces are shown. These two seem to agree very well qualitatively with only slight deviations. In addition, we observe the same features that have already been discussed in relation to figure 7.

To quantify these observations, we compute the p.d.f. of the locations of the T/NT interfaces in the  $y$  direction normal to the centreplane normalized by the vorticity thickness  $\delta_{\omega}$ , see figure 9. These p.d.f.s have been calculated for the upper (figure 9a) and lower (figure 9b) interface separately and are shown together with Gaussian distributions. Comparing the interface positions obtained from the vorticity and scalar interfaces, we observe a very good agreement between the locations from the two different approaches. Only in the tails do slight deviations occur; however, these are due to a very limited number of sample points leading to a reduced convergence.

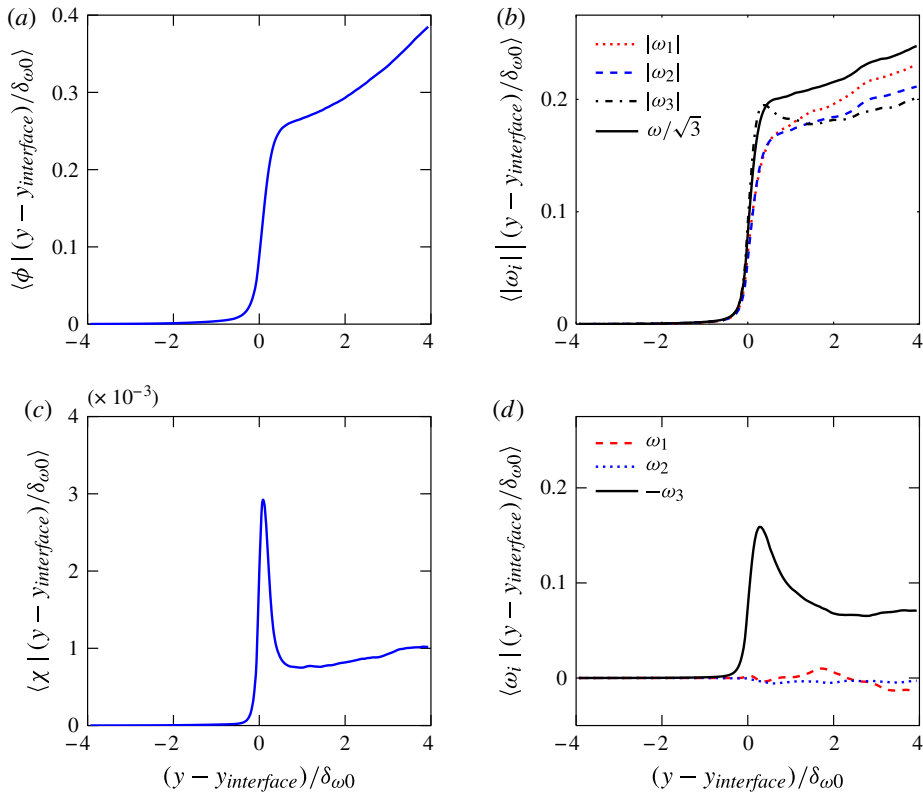


FIGURE 10. (Colour online) Comparison of conditional mean values across the (lower) scalar T/NT interface for (a) the passive scalar  $\phi$ , (b) the absolute value of vorticity  $\omega$  and its components, (c) the scalar dissipation rate  $\chi$  and (d) the components  $\omega_i$ .

A comparison between the DNS data and the normal distribution indicates a slight skewness towards the outer mixing layer region for both interfaces, in agreement with Westerweel *et al.* (2009) and Gampert *et al.* (2013a). The mean location of the T/NT interface for the upper interface is at  $y/\delta_{\omega 0} = 34.32$ , with a standard deviation  $\sigma$  of the p.d.f.  $\sigma = 3.54 \delta_{\omega 0}$ , and for the lower T/NT interface at  $y/\delta_{\omega 0} = 22.19$ , with a standard deviation of  $\sigma = 3.39 \delta_{\omega 0}$ .

#### 4.2. Mean profiles across the T/NT interfaces

In a next step, we investigate conditional mean profiles of various quantities in the cross-stream direction across the interface as illustrated in figure 8(a) meaning that the interface is always located at an abscissa value of zero. In figure 10 this conditional profile is shown for the passive scalar  $\phi$  (figure 10a), the absolute value of vorticity and the magnitude of its components (figure 10b), the scalar dissipation rate  $\chi$  (figure 10c) and the components of vorticity (figure 10d) based on the (lower) scalar interface. In agreement with Alexopoulos & Keffer (1971) and Westerweel *et al.* (2009), a steep rise of the scalar  $\phi$  across the interface can be observed in figure 10(a). This is followed by a small plateau, that Westerweel *et al.* (2009) have determined to be a characteristic length scale for the T/NT interface, which is assumed to be of the order of the Taylor microscale  $\lambda$ , in agreement with da Silva &

Taveira (2010) and Gampert *et al.* (2013a). This small plateau, however, is followed by an almost perfectly linear increase with respect to the distance from the interface into the turbulent flow region.

The same conditional profiles across the vorticity T/NT interface are shown in figure 10(b) for both the absolute values of vorticity and the single components  $|\omega_i|$ . Noticeably, the conditional mean of  $|\omega_3|$  is larger than  $|\omega_1|$  and  $|\omega_2|$  in the vicinity of the T/NT. Both the single components  $|\omega_i|$  as well as the absolute value of vorticity quickly decrease to an irrotational flow on the outside of the interface. The rest of the profile, however, closely follows the shape of the scalar  $\phi$  across the interface, i.e. we observe a sharp increase across the T/NT interface that is followed by an almost linearly increasing value for  $\omega$  in direction of the fully turbulent part. Westerweel *et al.* (2009) also report a jump in the value of the mean conditional vorticity and a nearly constant value of the vorticity on the inside of the interface that is also present in our data. The result that the mean conditional vorticity vanishes on the irrotational side of the interface and shows a strong jump at the interface also validates both approaches for the detection of the interface between the rotational and irrotational flow region. Westerweel *et al.* (2009) in addition interpret the peak at the interface to demonstrate the tendency of a vortex sheet to form at the outer edge of the shear flow. The peak in the mean conditional vorticity may alternatively be associated with small individual vortices with their axes normal to the plane of observation.

In contrast, the profile of the scalar dissipation rate (figure 10c) assumes an almost constant value in the fully turbulent region, which is followed by a strong peak at the T/NT interface and a decrease to an outer flow value of  $\chi = 0$ . Such a result is to be expected, as large scalar gradients are found at the interface (the scalar has to reach its turbulent (mean) value from a constant  $\phi = 0$  or  $\phi = 1$  in the non-turbulent region over a short distance, i.e. the interface thickness). Of course, large gradients may also occur in the turbulent core (scalar intermittency or cliff-ramp structures, see Warhaft 2000); however, the mean scalar dissipation is reduced by averaging over the entire turbulent core (i.e. it is diminished by large areas of small gradients). Obviously, this is not the case if averages are conditioned on the interface position.

Considering the instantaneous components, we observe in figure 10(d) that the conditional means of  $\omega_1$  and  $\omega_2$  are of higher-order small compared to  $\omega_3$ , which is the vorticity component in the spanwise  $z$  direction. Therefore, contributions of  $\omega_1$  and  $\omega_2$  but not  $\omega_3$  cancel out, which agrees very well with the symmetry of the flow configuration.

In §4.1, a very good agreement between the vorticity interface and the scalar interface has been found, which might be surprising as the absolute vorticity  $\omega = (\omega_i^2)^{1/2}$  is not a passive quantity like  $\phi$  but interacts with the flow. Comparing the respective governing equations,

$$\frac{\partial \phi}{\partial t} = -u_i \frac{\partial \phi}{\partial x_i} + \frac{1}{Pe_{\delta,0}} \frac{\partial^2 \phi}{\partial x_i^2}, \quad (4.1)$$

$$\frac{\partial \omega}{\partial t} = -u_j \frac{\partial \omega}{\partial x_j} + t_i^V \omega_j \frac{\partial u_i}{\partial x_j} + \frac{1}{Re_{\delta,0}} t_i^V \frac{\partial^2 \omega_i}{\partial x_j^2}, \quad (4.2)$$

where  $t_i^V = \omega_i / \omega$  is the unit vector tangential to the vorticity line, the vortex stretching term  $t_i^V \omega_j \partial u_i / \partial x_j$  stands out as a key difference. A collapse of the two interfaces thus requires a negligible vortex stretching at the interface. In figure 11(a,b), the balance of the respective governing equations conditioned on the distance from the lower

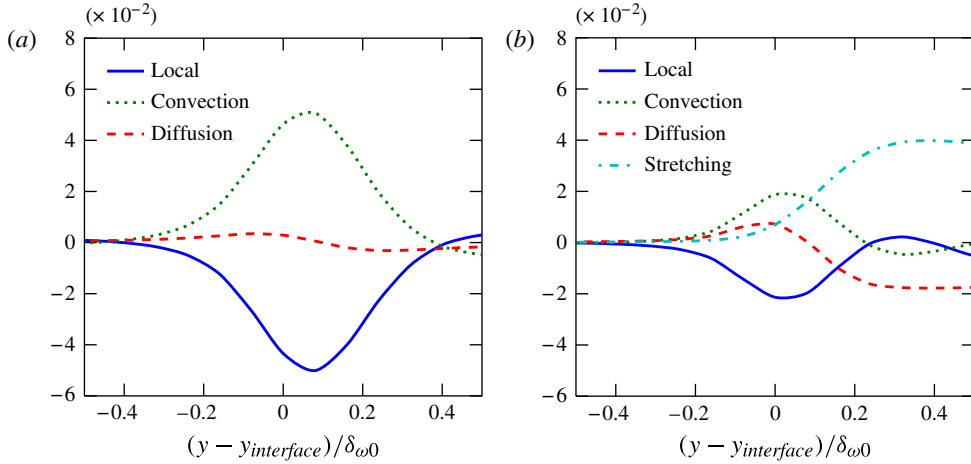


FIGURE 11. (Colour online) Comparison of conditional mean values of (a) (4.1) across the scalar interface, (b) (4.2) across the vorticity interface.

interface is shown. The lower interface has been chosen as in that case  $\phi = 0$  and  $\omega = 0$  in the outer flow. For the upper interface, the same characteristics are found, but as  $\phi = 1$  and  $\omega = 0$  in the outer flow, a rescaling of the passive scalar would be necessary. For the passive scalar (figure 11a), we find that the mean convective term  $u_i \partial \phi / \partial x_i$  peaks at the interface, while it vanishes in both the outer flow and the turbulent core region. The term  $(1/Pe_\delta) \partial^2 \phi / \partial x_i^2$  describes the diffusion of  $\phi$  in a coordinate frame attached to the interface, i.e. it equals the substantial derivative  $d\phi/dt = \partial \phi / \partial t + u_i \partial \phi / \partial x_i$ . It peaks on the irrotational side of the interface. Thereby, the passive scalar  $\phi$  (i.e. its threshold value) diffuses into the irrotational flow. We find the same behaviour for the vorticity balance, figure 11(b). Specifically, the vortex stretching term  $t_i^y \omega_j \partial u_i / \partial x_j$  is much smaller close to the interface than both the convective term  $u_j \partial \omega / \partial x_j$  and the diffusive term  $(1/Re_\delta) t_i^y \partial^2 \omega_i / \partial x_j^2$ . Only in the turbulent core region does the vortex stretching term dominate. The diffusive term can be interpreted as the projection of  $\nabla^2 \omega_i$  onto the vortex line and exhibits the same behaviour at the interface, i.e. vorticity diffuses from the interface into the outer irrotational flow, cf. Bisset *et al.* (2002). In the turbulent core region, this projection partly counteracts the vortex stretching and acts as a sink of vorticity. Overall, vortex stretching is not completely balanced by the diffusive projection in the turbulent core, so that there is a net production of vorticity  $\omega$ , leading to an expansion of the turbulent core into the irrotational region and providing the vorticity necessary for the interface to propagate by diffusion. This similarity of both the scalar and the vorticity equation at the respective interfaces in combination with their similar boundary conditions both in the irrotational and the turbulent region is responsible for the good agreement of the two interface detection criteria.

### 5. Orientation of vortex lines at the interface

After conditional statistics of various mean quantities across the vorticity and the scalar T/NT interfaces have been investigated, we now examine the p.d.f.s of the angle between the normal vector locally orthogonal to the T/NT interface and the unit vector attached to a vortex line.

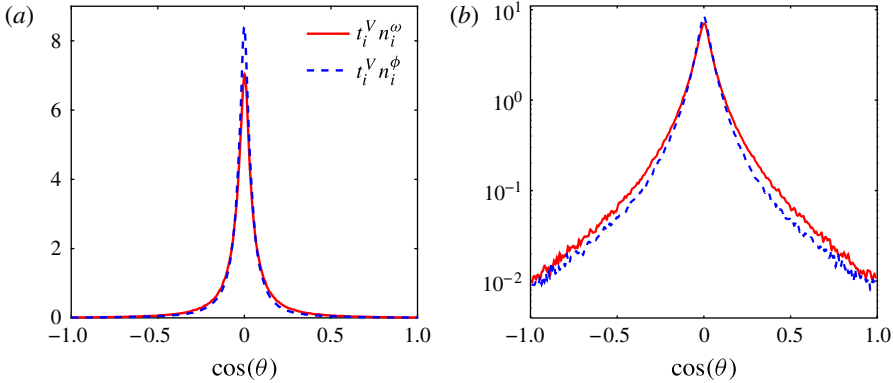


FIGURE 12. (Colour online) P.d.f. of  $\cos\theta$ , cosine of the angle between vortex lines and the unit normal of the vorticity interface, and of the angle between the lines and the scalar interface: (a) linear axis, (b) logarithmic axis.

We denote the unit vector perpendicular to the vorticity interface by  $n_i^\omega$  and the unit vector perpendicular to the scalar interface by  $n_i^\phi$ . Both  $n_i^\omega$  and  $n_i^\phi$  are defined to point towards the non-turbulent region. As  $\omega = 0$  in the non-turbulent zone and  $\omega = \omega_{turb} \neq 0$  in the turbulent core region, we have

$$n_i^\omega = -\frac{\partial\omega/\partial x_i}{|\nabla\omega|} \tag{5.1}$$

for both the upper and lower interface. On the other hand, as  $\phi = 0$  at the bottom and  $\phi = 1$  at the top of the domain, we define

$$n_i^\phi = \frac{\partial\phi/\partial x_i}{|\nabla\phi|} \tag{5.2}$$

for the upper and

$$n_i^\phi = -\frac{\partial\phi/\partial x_i}{|\nabla\phi|} \tag{5.3}$$

for the lower interface, ensuring that  $n_i^\phi$  is always pointing towards the non-turbulent zone.

In figure 12, the p.d.f. of  $\cos\theta = t_i^V n_i^\omega$  ( $t_i = \omega_i/\omega$  as introduced in § 4.2), i.e. the p.d.f. of the cosine of the angle between vortex lines and the unit vector perpendicular to the vorticity interface is shown, as well as the p.d.f. of  $\cos\theta = t_i^V n_i^\phi$  (the angle between the lines and the scalar interface). Statistics (mean, variance, skewness and flatness) of the orientation are found in table 2.

At the vorticity interface, the p.d.f. of the angle between vortex lines and the interface unit vector exhibits a very pronounced peak at  $\cos\theta = 0$ . Thus, vortex lines are parallel to the (vorticity) interface, cf. figure 13, and the resulting vortices entrain non-turbulent fluid into the turbulent flow, which is summarized as follows: as  $\omega = 0$  in the outer flow, vortex lines originating in the turbulent core cannot enter the non-turbulent region and are deflected at the (vorticity) interface, therefore ensuring the peak at  $\cos\theta = 0$ . Consequently near the T/NT interface, the component of vorticity normal to the isosurface is much smaller than the components parallel

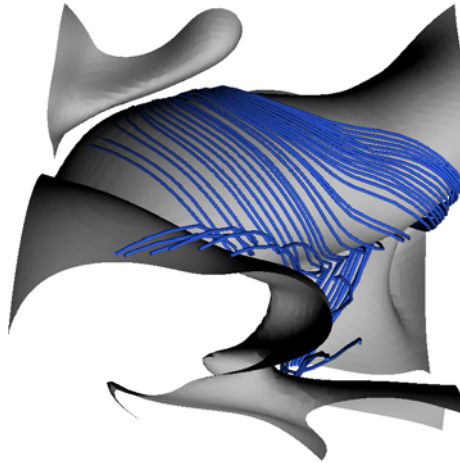


FIGURE 13. (Colour online) Vortex lines and vorticity interface isosurface.

	$\langle \theta \rangle$	$\sigma(\theta)$	$S(\theta)$	$F(\theta)$
$t_i^V n_i^\omega$	$4.988 \times 10^{-4}$	0.0287	$1.695 \times 10^{-5}$	$8.772 \times 10^{-3}$
$t_i^V n_i^\phi$	$-1.614 \times 10^{-3}$	0.0221	$-1.533 \times 10^{-4}$	$6.882 \times 10^{-3}$

TABLE 2. Mean, variance, skewness and flatness of  $\theta$  evaluated by the p.d.f. shown in figure 12(a,b).

to the isosurface, thus corrugating the T/NT interface and leading to entrainment (for more details on entrainment, see Mathew & Basu 2002 and Westerweel *et al.* 2009). Streamlines, on the other hand, may pass through the interface, as  $u_i \neq 0$  in the irrotational flow as well at the interface and the turbulent core, i.e. streamlines are everywhere well-defined.

Considering the scalar interface, the distribution of  $\cos \theta$  differs only slightly from the p.d.f.s at the vorticity interface, cf. figure 12; again, a distinct peak is found at  $\cos \theta = 0$  for vortex lines, i.e. the angle between vortex lines and the normal vector to the scalar interface exhibits the same distribution as in case of the vorticity interface. Such a similarity is to be expected, as both interfaces are located at the same position in space (cf. the p.d.f.s in figure 9a,b) and have a very similar shape as well, see figure 7.

Note that  $\cos \theta$  can also be interpreted as the ratio of the spatial change of  $\omega/\phi$  in the vortex line direction and the overall spatial change of that quantity at a point in space. This can easily be seen as

$$\cos \theta = t_i^V n_i = t_i^V \frac{\partial/\partial x_i}{|\nabla|} = \frac{\partial/\partial s}{|\nabla|}. \tag{5.4}$$

By definition,  $t_i^V \partial/\partial x_i = \partial/\partial s$ , where  $\partial/\partial s$  is the derivative in the vortex line direction. Thus,  $\cos \theta = 0$  implies that there is no change of  $\omega$  or  $\phi$  in the vortex line direction, whereas for  $\cos \theta = \pm 1$ , the direction of the gradient and the line coincide and  $\omega$  or  $\phi$  change the most in the line direction. Figure 12 implies that at the interface, there is only a very small change of both  $\omega$  and  $\phi$  in the vortex line direction, as the  $\omega/\phi$  isosurface is (nearly) parallel to the vortex lines.

## 6. Conclusion

We have performed a detailed comparison of the T/NT interface defined using either a vorticity or a scalar threshold. To this end, a DNS of a temporally evolving mixing layer has been analysed. The position p.d.f.s for both interfaces agree very well and are found to be Gaussian. In addition, the conditional statistics (conditional means of the vorticity and the passive scalar) are in good agreement with literature results (for instance, see Westerweel *et al.* 2009). Considering the scalar dissipation, a significant peak is observed if conditioned on the interface position, as assumed by Gampert *et al.* (2013a).

Next, we have investigated the terms of the governing equations for both the passive scalar and the vorticity conditioned on the distance to the respective interface isosurface. We find that the vortex stretching term is negligible at the interface and in its vicinity. Thus the transport equations for vorticity and the passive scalar are of similar nature close to the T/NT interface, i.e. both interfaces diffuse into the non-turbulent region. This similarity is responsible for the good agreement between both interface definitions and is also highlighted in the good collapse of the intermittency factors  $\gamma^\omega$  and  $\gamma^\phi$ .

The p.d.f.s of the angle between the unit tangent vector of vortex lines and the unit vector perpendicular to the respective vorticity or scalar interface have also been examined. In particular, the choice of the criteria defining the interface only results in small deviations; overall, very similar p.d.f.s are found for both the vorticity and scalar interface. Vortex lines are found to be perpendicular to the T/NT interface and the vortices induced by the vortex lines entrain non-turbulent outer flow. Such an orientation is to be expected, as a vanishing vorticity in the outer region confines vortex lines to the turbulent core (i.e. they may not pass the interface).

## Acknowledgements

This work was funded by the NRW-Research School ‘BrenaRo’ and the Cluster of Excellence ‘Tailor-Made Fuels from Biomass’, which is funded by the Excellence Initiative of the German federal state governments to promote science and research at German universities.

## REFERENCES

- ALEXOPOULOS, C. C. & KEFFER, J. F. 1971 Turbulent wake in a passively stratified field. *Phys. Fluids* **14**, 216–224.
- ASHURST, W. T., KERSTEIN, A. R., KERR, R. M. & GIBSON, C. H. 1987 Alignment of vorticity and scalar gradient with strain rate in simulated Navier–Stokes turbulence. *Phys. Fluids* **30**, 2343–2353.
- BISSET, D., HUNT, J. & ROGERS, M. 2002 The turbulent/non-turbulent interface bounding a far wake. *J. Fluid Mech.* **451**, 383–410.
- BROWN, G. & ROSHKO, A. 1974 On density effects and large structure in turbulent mixing layers. *J. Fluid Mech.* **64**, 775–816.
- BUCH, K. A. & DAHM, W. J. 1996 Experimental study of the fine-scale structure of conserved scalar mixing in turbulent shear flows. Part 1.  $Sc > 1$ . *J. Fluid Mech.* **317**, 21–71.
- BUCH, K. A. & DAHM, W. J. 1998 Experimental study of the fine-scale structure of conserved scalar mixing in turbulent shear flows. Part 2.  $Sc \approx 1$ . *J. Fluid Mech.* **364**, 1–29.
- CANNON, S., CHAMPAGNE, E. & GLEZER, A. 1993 Observations of large-scale structures in wakes behind axisymmetric bodies. *Exp. Fluids* **14**, 447–450.

- CHONG, M., PERRY, A. & CANTWELL, B. 1990 A general classification of three-dimensional flow fields. *Phys. Fluids A* **2**, 408–420.
- DIMOTAKIS, P., MIAKE-LYE, R. & PAPANTONIOU, D. A. 1983 Structure and dynamics of round turbulent jets. *Phys. Fluids* **26**, 3185–3192.
- FRANK, J. H. & KAISER, S. A. 2010 High-resolution imaging of turbulence structures in jet flames and non-reacting jets with laser Rayleigh scattering. *Exp. Fluids* **49** (4), 823–837.
- GAMPERT, M., KLEINHEINZ, K., PETERS, N. & PITSCH, H. 2014 Experimental and numerical study of the scalar turbulent/non-turbulent interface layer in a jet flow. *Flow Turbul. Combust.* **92** (1–2), 429–449.
- GAMPERT, M., NARAYANASWAMY, V., SCHAEFER, P. & PETERS, N. 2013a Conditional statistics of the turbulent/non-turbulent interface in a jet flow. *J. Fluid Mech.* **731**, 615–638.
- GAMPERT, M., SCHAEFER, P., NARAYANASWAMY, V. & PETERS, N. 2013b Gradient trajectory analysis in a jet flow for turbulent combustion modelling. *J. Turbul.* **14**, 147–164.
- GRANT, H. 1958 The large eddies of turbulent motion. *J. Fluid Mech.* **4**, 149–190.
- HOLZNER, M., LIBERZON, A., NIKITIN, N., KINZELBACH, W. & TSINOBER, A. 2007a Small-scale aspects of flows in proximity of the turbulent/non-turbulent interface. *Phys. Fluids* **19** (7), 071702.
- HOLZNER, M., LIBERZON, A., NIKITIN, N., LÜTHI, B., KINZELBACH, W. & TSINOBER, A. 2008 A Lagrangian investigation of the small-scale features of turbulent entrainment through 3D-PTV and DNS. *J. Fluid Mech.* **598**, 465–475.
- HOLZNER, M., LUETHI, B., TSINOBER, A. & KINZELBACH, W. 2007b Acceleration, pressure and related quantities in the proximity of the turbulent/non-turbulent interface. *J. Fluid Mech.* **639**, 153–165.
- HUNT, J., EAMES, I., DA SILVA, C. & WESTERWEEL, J. 2011 Interfaces and inhomogeneous turbulence. *Phil. Trans. R. Soc. Lond. A* **369**, 811–832.
- HUSSAIN, A. 1986 Coherent structures and turbulence. *J. Fluid Mech.* **173**, 303–356.
- JIMENEZ, J., WRAY, A. A., SAFFMANN, P. G. & ROGALLO, R. 1993 The structure of intense vorticity in isotropic turbulence. *J. Fluid Mech.* **255**, 65–90.
- KERR, R. M. 1985 Higher-order derivative correlations and the alignment of small-scale structures in isotropic numerical turbulence. *J. Fluid Mech.* **153**, 31–58.
- KLINE, S., REYNOLDS, W., SCHRAUB, F. & RUNSTADLER, P. 1967 The structure of turbulent boundary layers. *J. Fluid Mech.* **30**, 741–773.
- KUSHNIR, D., SCHUMACHER, J. & BRANDT, A. 2006 Geometry of intense scalar dissipation events in turbulence. *Phys. Rev. Lett.* **97**, 124502.
- LELE, S. 1992 Compact finite difference schemes with spectral-like resolution. *J. Comput. Phys.* **103**, 16–42.
- LIEPMANN, D. & GHARIB, M. 1992 The role of streamwise vorticity in the near-field entrainment of round jets. *J. Fluid Mech.* **245**, 643–668.
- MARUSIC, I. & ADRIAN, R. A. 2011 The eddies and scales of wall turbulence. In *Ten Chapters in Turbulence* (ed. Y. Kaneda, P. Davidson & K. R. Sreenivasan), Cambridge University Press.
- MARUSIC, I. & PERRY, A. 1995 A wall-wake model for the turbulence structure of boundary layers. Part 2. Further experimental support. *J. Fluid Mech.* **298**, 389–407.
- MATHEW, J. & BASU, A. 2002 Some characteristics of entrainment at a cylindrical turbulence boundary. *Phys. Fluids* **14**, 2065–2072.
- MELLADO, J. P., WANG, L. & PETERS, N. 2009 Gradient trajectory analysis of a scalar field with internal intermittency. *J. Fluid Mech.* **626**, 333–365.
- NICKELS, T. & PERRY, A. 1996 An experimental and theoretical study of the turbulent coflowing jet. *J. Fluid Mech.* **309**, 157–182.
- PANTANO, C. & SARKAR, S. 2002 A study of compressibility effects in the high-speed turbulent shear layer using direct simulation. *J. Fluid Mech.* **451**, 329–371.
- PATTON, R., GABET, K., JIANG, N., LEMPERT, W. & SUTTON, J. 2012 Multi-kHz mixture fraction imaging in turbulent jets using planar Rayleigh scattering. *Appl. Phys. B* **106**, 457–471.
- PERRY, A. & CHONG, M. 1982 On the mechanism of wall turbulence. *J. Fluid Mech.* **119**, 173–217.

- PHILIP, J. & MARUSIC, I. 2012 Large-scale eddies and their role in entrainment in turbulent jets and wakes. *Phys. Fluids* **24** (5), 055108.
- PRASAD, R. R. & SREENIVASAN, K. R. 1989 Scalar interfaces in digital images of turbulent flows. *Exp. Fluids* **7**, 259–264.
- ROGERS, M. & MOSER, R. 1994 Direct numerical simulation of a self-similar turbulent mixing layer. *Phys. Fluids* **6**, 903–923.
- RUETSCH, G. R. & MAXEY, M. R. 1991 Small-scale features of vorticity and passive scalar fields in homogeneous isotropic turbulence. *Phys. Fluids A* **3**, 1587–1597.
- DA SILVA, C. B. & DOS REIS, R. J. N. 2011 The role of coherent vortices near the turbulent/non-turbulent interface in a planar jet. *Phil. Trans. R. Soc. Lond. A* **369** (1937), 738–753.
- DA SILVA, C. B. & PEREIRA, J. C. 2008 Invariants of the velocity-gradient, rate-of-strain, and rate-of-rotation tensors across the turbulent/non-turbulent interface in jets. *Phys. Fluids* **20**, 055101.
- DA SILVA, C. B. & TAVEIRA, R. R. 2010 The thickness of the turbulent/non-turbulent interface is equal to the radius of the large vorticity structures near the edge of the shear layer. *Phys. Fluids* **22**, 121702.
- SREENIVASAN, K. R. & MENEVEAU, C. 1986 The fractal facets of turbulence. *J. Fluid Mech.* **173**, 357–386.
- SU, L. K. & CLEMENS, N. T. 2003 The structure of fine-scale scalar mixing in gas-phase planar turbulent jets. *J. Fluid Mech.* **488**, 1–29.
- TAVEIRA, R. R. & DA SILVA, C. B. 2013 Kinetic energy budgets near the turbulent/non-turbulent interface in jets. *Phys. Fluids* **25**, 015114.
- TOWNSEND, A. A. 1948 Local isotropy in the turbulent wake of a cylinder. *Austral. J. Sci. Res. A* **1** (2), 161–174.
- TOWNSEND, A. A. 1949 The fully developed turbulent wake of a circular cylinder. *Austral. J. Sci. Res. A* **2** (4), 451–468.
- TOWNSEND, A. A. 1956 *The Structure of Turbulent Shear Flow*. Cambridge University Press.
- TOWNSEND, A. A. 1966 The mechanism of entrainment in free turbulent flows. *J. Fluid Mech.* **26**, 689–715.
- TOWNSEND, A. A. 1987 Organized eddy structures in turbulent flows. *Physico-Chem. Hydrodyn.* **8** (1), 23–30.
- TSINOBER, A., ORTENBERG, M. & SHTILMAN, L. 1999 On depression of nonlinearity in turbulence. *Phys. Fluids* **11**, 2291–2297.
- TSINOBER, A., SHTILMAN, L. & VAISBURD, H. 1997 A study of properties of vortex stretching and enstrophy generation in numerical and laboratory turbulence. *Fluid Dyn. Res.* **21** (6), 477–494.
- VINCENT, A. & MENEGUZZI, M. 1994 On the dynamics of vorticity tubes in homogeneous turbulence. *J. Fluid Mech.* **258**, 245–254.
- WARHAFT, Z. 2000 Passive scalars in turbulent flows. *Annu. Rev. Fluid Mech.* **32**, 203–240.
- WATANABE, T. & GOTOH, T. 2004 Statistics of a passive scalar in homogeneous turbulence. *New J. Phys.* **6** (40), 010040.
- WESTERWEEL, J., FUKUSHIMA, C., PEDERSEN, J. & HUNT, J. 2005 Mechanics of the turbulent non-turbulent interface of a jet. *Phys. Rev. Lett.* **95**, 174501.
- WESTERWEEL, J., FUKUSHIMA, C., PEDERSEN, J. & HUNT, J. 2009 Momentum and scalar transport at the turbulent/non-turbulent interface of a jet. *J. Fluid Mech.* **631**, 199–230.
- WESTERWEEL, J., HOFMANN, T., FUKUSHIMA, C. & HUNT, J. 2002 The turbulent/non-turbulent interface at the outer boundary of a self-similar turbulent jet. *Exp. Fluids* **33**, 873–878.
- WESTERWEEL, J., PETRACCI, A., DELFOS, R. & HUNT, J. 2011 Characteristics of the turbulent/non-turbulent interface of a non-isothermal jet. *Phil. Trans. R. Soc. Lond. A* **369**, 723–737.
- YODA, M., HESSELINK, L. & MUNGAL, M. G. 1994 Instantaneous three-dimensional concentration measurements in the self-similar region of a round high-Schmidt-number jet. *J. Fluid Mech.* **279**, 313–350.